Draft version October 31, 2025
Typeset using LaTeX default style in AASTeX7.0.1

Rotation Measure Analysis of Shocks and Sloshing Fronts in a Galaxy Cluster Merger Simulation

J.-R. Liou,[1] Alvina Y. L. On,[2,3,4] H.-Y. Karen Yang[2,5] And J. A. ZuHone[6]

[1]Department of Physics, National Tsing Hua University, Hsinchu, Taiwan
[2]Physics Division, National Center for Theoretical Sciences, Taipei, 106319, Taiwan
[3]Center of Theory and Computation, National Tsing Hua University, Hsinchu 30013, Taiwan
[4]Mullard Space Science Laboratory, University College London, Holmbury St. Mary, Surrey RH5 6NT, United Kingdom
[5]Institute of Astronomy, National Tsing Hua University, Hsinchu, 30013, Taiwan
[6]Harvard-Smithsonian Center for Astrophysics, Cambridge, MA 02138, USA

ABSTRACT

Recent observations of the Fornax cluster show depolarization signatures on megaparsec scales, which may be associated with shocks and/or sloshing motions during cluster merger and/or in-fall. To investigate the possible reasons behind the depolarization, we carry out analytical and full polarized radiative transfer (PRT) calculations of radio point sources behind a merging galaxy cluster simulated using the FLASH code. With uniform background light, we analyzed the rotation measure (RM) morphology near the shock front and the cluster center, where sloshing cold fronts appear. For the shock scenario, we find a local RM enhancement by $\sim 56\%$ behind the shock front on megaparsec scales, arising from the compression of hot gas and magnetic field lines. Behind the sloshing cold front, the cluster center shows decrement in RM magnitude by $\sim 23.3\%$, as a result of the cancellation effect of randomly-oriented magnetic fields induced by sloshing-driven turbulence. We find that beam depolarization increases behind shock fronts and across sloshing cold fronts, indicating enhanced magnetic field fluctuations across the plane of the sky in both scenarios. By fully accounting for all radiative transfer coefficients in the PRT calculations, the uniform background light becomes more depolarized near the cluster center, with the effect growing more pronounced as background intensity decreases. This suggests that synchrotron emission and Faraday rotation of the intracluster medium can significantly influence the polarization of background sources.

Keywords: magnetic fields — polarization – radiative transfer – galaxies: clusters: intracluster medium – methods: data analysis – radiation mechanism: non-thermal

1. INTRODUCTION

Magnetic fields in the intracluster medium (ICM), though typically dynamically subdominant on large scales, could play a vital role in delaying the onset of hydrodynamic instabilities and stabilizing interfaces of discontinuities such as merger-induced cold fronts. However, direct observation of large-scale magnetic fields and their structures in the ICM remains challenging, as these fields are weak. Therefore, indirect methods are often used to infer the properties of the large-scale magnetic fields (see reviews by C. L. Carilli & G. B. Taylor 2002; C. Ferrari et al. 2008; L. M. Widrow 2002). A common method is the projected rotation measure (RM), which probes the magnetic field strength along the line of sight via the Faraday rotation effect. Faraday rotation causes the polarization plane of linearly polarized light to rotate by an angle $\Delta\varphi = \mathrm{RM}\lambda^2$, where λ is the observed wavelength, due to the differing phase velocities of right- and left-handed circularly polarized waves. The RM depends on the product of the thermal electron number density and the magnetic field strength along the line of sight.

Typically, RM measurements from extragalactic radio sources passing through the intergalactic medium (IGM) yield values of only a few rad m^{-2}, even though they can reach several hundreds near the Galactic plane due to the influence of the denser, magnetized interstellar medium (M. Simard-Normandin & P. P. Kronberg 1980; C. L. Carilli & G. B. Taylor 2002; S. Hutschenreuter et al. 2022). In contrast, some radio galaxies like Cygnus A exhibit much steeper RM gradients and significantly higher RM values, while its polarization fraction remains constant. This behavior strongly suggests that the enhanced RM observed near

Email: alex0106@gapp.nthu.edu.tw (JRL), alvina.on@ucl.ac.uk (AYLO), hyang@phys.nthu.edu.tw (HYKY), john.zuhone@cfa.harvard.edu (JAZ)

central radio sources in galaxy clusters arises from a foreground screen of dense, magnetized intracluster gas acting as a Faraday screen, rather than from thermal gas intermixed with the synchrotron-emitting plasma. If the latter were the case, strong internal Faraday rotation would cause significant depolarization at lower frequencies. This effectively rules out both Galactic contributions and internal Faraday rotation as dominant sources of the observed RM in these systems (S. Mitton 1971; J. W. Dreher et al. 1987; T. E. Clarke et al. 2001). Therefore, RM of background sources behind galaxy clusters could be an effective probe for magnetic structures in the ICM.

During hierarchical structure formation, the merger and accretion of galaxy clusters generate large-scale shocks that transport energy and propagate through the ICM at speeds exceeding the local sound speed. Owing to the relatively high sound speed in the hot ICM, these shocks are typically weak, with Mach numbers on the order of 1.5–3 (D. Ryu et al. 2003; J.-H. Ha et al. 2018). However, such shocks can significantly affect the cluster environment. They compress the component of the magnetic field parallel to the shock surface while leaving the perpendicular component largely unchanged, thereby amplifying and aligning magnetic fields along their surfaces. Furthermore, the shock itself generates vorticity, which can further cascade into turbulence and tangle magnetic fields in the downstream (U. Keshet et al. 2010; R. J. van Weeren et al. 2010; L. Iapichino & M. Brüggen 2012; M. Brüggen et al. 2012; C. S. Anderson et al. 2021).

In contrast, gas sloshing in clusters arises from large-scale motions of the ICM within the gravitational potential, often triggered by the infall of a subcluster or galaxy. This process produces cold fronts—sharp contact discontinuities in density and temperature—which can drive shear flows that stretch and amplify magnetic fields carried with the gas due to the magnetic field draping effect (M. Lyutikov 2006; J. A. ZuHone et al. 2011). The interface of the cold front is susceptible to hydrodynamic instabilities that, at later stages, induce turbulence that distorts and randomizes the field orientation (P. Schuecker et al. 2004). Such turbulence can lead to depolarization, as fluctuations in field direction cause cancellation of polarized emission along the line of sight (C. L. Carilli & G. B. Taylor 2002; B. J. Burn 1966; D. D. Sokoloff et al. 1998; M. Murgia et al. 2004; A. Bonafede et al. 2010; C. S. Anderson et al. 2021; S. Sur et al. 2021).

A recent study of the Fornax cluster by C. S. Anderson et al. (2021) identified a bow-shaped enhancement in Faraday depth (FD) (Section 2.2) on the southwest side of the cluster, with a swept-back feature extending northeast, resembling the signature of a shock front. This suggests that dynamical activity in the ICM may have introduced discontinuities in density and reorienting magnetic field lines into a more ordered structure. Additionally, an uneven mass distribution between the main cluster and the southwestern subcluster Fornax A (NGC1316) has been reported (M. J. Drinkwater et al. 2001). A series of merger events, including the infall of NGC1404, are believed to have triggered sloshing and merger-driven shocks on scales exceeding several degrees (1° = 360kpc) (M. Machacek et al. 2005; Y. Su et al. 2017b; Y. Su et al. 2017; A. Sheardown et al. 2018; C. S. Anderson et al. 2021). The latest MeerKAT Fornax Survey F. Loi et al. (2025) further supports these findings, showing an increase in RM scatter beyond 300 kpc from the cluster center, and revealing a previously undetected high-RM stripe extending from north to south-southwest. Together, these observations underline the utility of RM as a powerful diagnostic tool for investigating the magnetic field structure within galaxy clusters.

C. S. Anderson et al. (2021) suggests that the enhanced RM corresponds to a shock front, and that a slightly offset contact discontinuity separates a triangular extension of elevated RM values in the northeast. They propose that this entire feature may result from turbulence eddies generated by a northeast–southwest subcluster merger. Curiously, there is a narrow zone where the polarized background source counts is reduced and the RM values are comparatively lower. This region may contain turbulence that tangles magnetic field lines, resulting in depolarization (B. J. Burn 1966; D. D. Sokoloff et al. 1998; M. Murgia et al. 2004). The asymmetric, swept-back X-ray morphology toward the northeast in Chandra data, and possibly in ROSAT once accounting for smoothing and contamination from point sources, both hint at merger activities (C. Jones et al. 1997; C. A. Scharf et al. 2005; C. S. Anderson et al. 2021). These images also reveal edges consistent with cold fronts at radii of several hundred kiloparsecs – features believed to result from gas sloshing triggered by the infall of NGC 1404 (Y. Su et al. 2017b; Y. Su et al. 2017). C. S. Anderson et al. (2021) proposes that the region lacking polarized background sources may result from small-scale structures in the ICM depolarizing the emission. These small-scale magnetic structures are often generated by turbulence, which commonly arises between shock fronts and contact discontinuities, or underneath sloshing cold fronts. Motivated by this connection, we aim to use simulations to interpret the observed depolarization and its relation to turbulence-driven magnetic field fluctuations.

The Fornax cluster is a nearby, low-mass, cool-core system located at a distance of $\sim$19 Mpc, centered on the galaxy NGC 1399 in the southern sky at redshift $z = 0.00475$. Despite its proximity, no diffuse radio halo has been detected (L. Bîrzan et al. 2012). X-ray observations provide important insights into the cluster's core and inner regions, but the currently available data do not reach the cluster outskirts with sufficient depth to probe for shocks on larger scales (Y. Su et al. 2017; F. Loi et al. 2025). This limitation is particularly relevant in light of the bow-shaped RM feature identified by C. S. Anderson et al. (2021), which may trace a shock front extending into the outer regions of the ICM. Regardless, two radio jets are seen protruding from opposite ends of the central galaxy NGC1399 at the cluster core, rising up to 10 kiloparsecs (K. Shurkin et al. 2008; J. I. Davies et al. 2013; Y. Su et al. 2017a; Y. Su et al. 2017). Moreover, further studies show disturbance in the ICM with asymmetric X-ray and metallicity distribution, and the morphology in the FD pattern (Y. Su et al. 2017a; C. S. Anderson et al. 2021) all points to a disturbed system. It is still unclear how the polarized properties of the Fornax cluster is influenced by the complex effects of shocks and cold fronts during the merger activities. The point sources observed in Fornax are primarily background active galactic nuclei (AGN) located behind the cluster field-of-view (e.g., M. E. Machacek et al. 2005; C. S. Anderson et al. 2021). These sources, while not physically associated with the cluster, serve as useful probes of the ICM through Faraday rotation and depolarization effects.

In this paper, we focus on analyzing RM maps of shock and sloshing scenarios in the ICM, and try to reconcile with the signatures seen in the Fornax observations. To quantify these RM effects, we carry out analytical and full PRT calculations of radio point sources behind a merging galaxy cluster simulated using the FLASH code (B. Fryxell et al. 2000). In the analytical approach, we assume that Faraday rotation dominates the polarization behavior in the ICM – as is the case for most Faraday-thin objects – and that the RM at each location is the cumulative Faraday effect of the line-of-sight magnetic field strength and thermal electron number density. We also compared our analytical results to full PRT calculations that account for absorption, Faraday conversion, and the contribution from non-thermal electrons.

The paper is organized as follows. In Section 2, we introduce the simulation of a binary cluster merger, in which an infalling subcluster generates shock waves and later induces a gas sloshing event (Section 2.1). We want to look specifically at how shocks and sloshing reshape the RM and polarization structure. We go beyond RM by solving the full PRT equation, which tracks how polarized light evolves through the ICM, accounting for emission, absorption, and Faraday rotation (Section 2.2). We then simplify the model under the assumption of dominant Faraday rotation. We outline the analytical formalisms we apply to compute the polarization and projected X-ray emissivity in Section 2.3. In Section 3, we present the results of our analysis, focusing on the RM and beam-smoothing effects associated with the shock and sloshing scenarios (Sections 3.1 and 3.2, respectively). We compare polarization signatures derived from the PRT equations across different physical conditions, emphasizing their implications for magnetic field structures and their connection to the observed polarization of background light (Section 3.3). In Section 4, we discuss the limitations of both the simulation and analytical approaches, and relate our findings to observational data where possible. Finally, in Section 5, we summarize the main conclusions of this work.

2. METHOD

2.1. *Galaxy Cluster Merger Simulation using FLASH*

To understand the effects of shocks and sloshing on the distribution of magnetic fields, gas, and in turn the projected polarization signals, we analyze one magneto-hydrodynamic (MHD) binary cluster merger simulation adapted from J. A. ZuHone et al. (2011) using the FLASH code (A. Dubey et al. 2009; E. Roediger & J. A. Zuhone 2012). The merger simulation is carried out in a box with a length of $L = 8$ Mpc, and is comprised of the merger of two clusters on the $x - y$ plane with a 5:1 mass ratio. The infalling subcluster is represented by a dark matter (DM) halo devoid of gas. The initial separation and impact parameter are 3 Mpc and 0.5 Mpc, respectively, and the subcluster itself is moving in the (-x)-direction at 1466 km/s initially. While the main cluster has a mass comparable to the Perseus cluster, the properties of shocks and sloshing signatures generated in this simulation are chiefly determined by the mass ratio and impact parameter, thus not sensitive to the cluster masses.

The adaptive mesh refinement (AMR) method of the FLASH code, which is based on the second order derivative of density, allows us to have a finer resolution at the region of interest where shocks and sloshing are taking place. The gas is set as an ideal fluid with an adiabatic index of 5/3, and for simplicity, there is no viscosity included in the run. The initial profile of the dark matter follows the Navarro–Frenk–White profile (NFW profile) (J. F. Navarro et al. 1997), and their velocity distribution is initialized by the Eddington formula (A. S. Eddington 1916). The gravitational potential is determined by the dark matter, which is represented by a group of collisionless particles, and their dynamics are computed by an N-body scheme in the FLASH code. Lastly, the magnetic field is initialized as a tangled field with a Kolmogorov power spectrum. The spectrum includes cutoffs at both low and high spatial scales: the lower cutoff corresponds to 500 kpc, while the higher cutoff corresponds to 43 kpc (J. A. ZuHone et al. 2013). The field strength is normalized to an approximately uniform plasma beta of $\beta = p_{\rm gas}/p_{\rm B} = 100$ (F. Govoni et al. 2010; J. A. ZuHone et al. 2011).

The evolution of the cluster merger process is briefly described as follows. Since the subcluster itself is not equipped with gas, to track its position, we identify the subcluster by the local minimum of the gravitational potential away from the cluster center. Viewed along the z direction, a subcluster comes from the upper right side at $[3, 0.5, 0]$ Mpc towards the lower left side of the simulation box. At time $t = 2$ Gyr, the merging event of the subcluster at high speed through the ICM produces a discontinuous density jump across the shock front at about $[-1.1, -0.5, 0]$ Mpc, leaving a wake of disturbed gas behind. After the subcluster passes through the cluster center at $t = 2.7$ Gyr, the gas starts to slosh around the gravitationally perturbed DM potential of the main cluster, lagging behind slightly due to the ram pressure it experiences. Since the sloshing gas in the outer layer is hardly mixed with the center because of their density and temperature differences, there are discontinuities in electron density and temperature, forming the so-called "cold fronts".

2.2. *The Polarized Radiative Transfer (PRT) Equations and Rotation Measure (RM)*

In the local frame, the PRT equations can be written as

$$\frac{d}{ds}\begin{bmatrix} I_\nu \\ Q_\nu \\ U_\nu \\ V_\nu \end{bmatrix} = -\begin{bmatrix} \kappa_\nu & q_\nu & u_\nu & v_\nu \\ q_\nu & \kappa_\nu & f_\nu & -g_\nu \\ u_\nu & -f_\nu & \kappa_\nu & h_\nu \\ v_\nu & g_\nu & -h_\nu & \kappa_\nu \end{bmatrix}\begin{bmatrix} I_\nu \\ Q_\nu \\ U_\nu \\ V_\nu \end{bmatrix} + \begin{bmatrix} \epsilon_{\mathrm{I},\nu} \\ \epsilon_{\mathrm{Q},\nu} \\ \epsilon_{\mathrm{U},\nu} \\ \epsilon_{\mathrm{V},\nu} \end{bmatrix} \tag{1}$$

(see e.g. A. G. Pacholczyk 1970, 1977; T. W. Jones & S. L. O'Dell 1977), where $[I_\nu, Q_\nu, U_\nu, V_\nu]$ are the Stokes parameters at a specific frequency ν propagating along the distance s, with the coefficients κ_ν, q_ν, u_ν, v_ν for absorption, f_ν for Faraday rotation, g_ν and h_ν for Faraday conversion, and ϵ_ν for emission (see also A. Y. L. On et al. 2019; J. Y. H. Chan et al. 2019, for a summary). The scattering term is neglected in this work for the diffuse ICM. Hereafter, the subscript ν is omitted for simplicity and the specific Stokes parameters are now written as $[I, Q, U, V]$. The polarization angle is defined in terms of $\varphi = 0.5\tan^{-1}(U/Q)$, while the degree of linear polarization (DOLP) is $\Pi_{\mathrm{L}} = \left(\sqrt{Q^2 + U^2}\right)/I$.

Neglecting absorption, emission and circular polarization, equation 1 can be simplified into

$$\frac{d}{ds}\begin{bmatrix} Q \\ U \end{bmatrix} = -\begin{bmatrix} 0 & f \\ -f & 0 \end{bmatrix}\begin{bmatrix} Q \\ U \end{bmatrix}. \tag{2}$$

In most galaxy clusters, the Faraday rotation is mainly contributed by the thermal electrons (H. Kotarba et al. 2011), such that

$$f_{\mathrm{th}} = \frac{1}{\pi}\left(\frac{e^3}{m^2c^4}\right) n_{\mathrm{e,th}}\, B_\parallel\, \lambda^2, \tag{3}$$

where e is the electron charge, m is the mass of the electron, c is the speed of light, $n_{\mathrm{e,th}}$ is the number density of the thermal electrons, and $B_\parallel$ is the magnetic field strength along the line of sight.

Substituting equation 3 into 2 gives

$$\varphi = \varphi_0 + \frac{2\pi e^3}{m^2(c\omega)^2}\int_{\mathrm{source}}^{\mathrm{observer}} n_{\mathrm{e,th}}(\mathrm{s}')\mathrm{B}_\parallel(\mathrm{s}')\,\mathrm{ds}', \tag{4}$$

where φ_0 is the intrinsic polarization angle of the source. The observed FD is acquired by identifying the peak in the Faraday dispersion function (intrinsic polarized flux as a function of the FD). When there is only a single source along the line of sight, RM is then equivalent to the corresponding FD value at the peak of the Farady dispersion function, and the two terms are interchangeable (G. Heald 2009). Thus, in this context, the RM is computed by

$$\mathrm{RM} = (\varphi - \varphi_0)\,\lambda^{-2} \tag{5}$$

$$\approx 0.812\int_{\mathrm{source}}^{\mathrm{observer}}\left(\frac{\mathrm{n_{e,th}(s')}}{\mathrm{cm^{-3}}}\right)\left(\frac{B_\parallel(\mathrm{s}')}{\mu\mathrm{G}}\right)\left(\frac{\mathrm{ds}'}{\mathrm{pc}}\right)\,\mathrm{rad\ m^{-2}}, \tag{6}$$

where we set $\lambda \approx 0.21$ m at 1.4 GHz in our calculations.

To compute polarization signatures, we performed post-processing on simulation snapshots at chosen redshifts. We constructed a pipeline for the PRT analysis by generating a 3D grid (256^3 cells) of thermal electron number density, temperature, and magnetic field within the simulation domain. These inputs were used by the PRT code to compute local transfer coefficients. The coupled PRT equations were integrated using a fourth-order Runge-Kutta method, with initial Stokes parameters $[I, Q, U, V]$ specified at the first slice and propagated through the domain to the final plane.

2.3. *Calculation of the Synthetic X-ray and Radio Maps*

To investigate the distribution of gas density and magnetic fields in the ICM during a merger, we construct synthetic X-ray and radio maps. Their corresponding two-dimensional maps are generated by projecting the X-ray and radio emissivities along a given line of sight. For the X-ray component, we calculate the projected emissivity in the energy range 0.5–7 keV using version 13.vr of Cloudy (last described by G. J. Ferland et al. (2013)), coupled with the astrophysical visualization and analysis toolkit yt (see more details on the astrophysical visualization toolkit from M. J. Turk et al. 2011), assuming gas with a constant $0.3Z_{\odot}$. For the radio emissivity we assume that the relativistic electrons have a power-law energy spectrum and calculate the total radio emissivity following the approach in D. J. Barnes et al. (2018). Here we assume that the Lorentz factor of the low energy electron cut-off is $\gamma = 10^3$ and their energy density is one percent of the thermal energy density. In terms of radio polarization, the complex linear polarization $\mathbf{P}$ can be expressed in terms of the normalized Stokes parameters Q and U, and hence can be written as

$$\mathbf{P} = p \exp(i2\varphi) = p(\cos(2\varphi) + i \sin(2\varphi)) \,, \tag{7}$$

where p is the degree of linear polarization $\Pi_{\rm L}$ of the background light.

In Sections 3.1 and 3.2, we assume that the intervening cluster predominantly contributes to Faraday rotation only and does not emit any radio synchrotron radiation. For simplicity, we consider a uniform background of radio point sources where we assume that every point source has $U = 0$ and $Q = I$, such that their initial polarization angle is $\varphi_0 = 0$ and $\Pi_{\rm L} = 1$. The intervening cluster can be treated as a random external Faraday screen and the resulting complex linear polarization is then

$$\mathbf{P} = \mathbf{P}_{\rm int}\, \mathbf{P}_{\rm ext} \tag{8}$$

(D. D. Sokoloff et al. 1998), where $\mathbf{P}_{\rm int}$ is the intrinsic complex polarization of the background light source.

The complex polarization of the external Faraday screen is

$$\mathbf{P}_{\rm ext} = \langle\, \exp\,(2i\; {\rm RM}\; \lambda^2)\, \rangle_w , \tag{9}$$

where $\langle ... \rangle$ is the spatial averaging over the telescope beam size w. The spatial averaging of polarization signals is similar to the smearing of signals by a telescope with a finite resolution, which is also known as beam depolarization. We assume a Gaussian beam in our calculations.

3. RESULTS

3.1. *Shock Scenario*

We present the RM maps of the merging cluster and examine how the polarization of the uniform background light changes as the merger evolves. For both the shock and sloshing scenarios, in Sections 3.1 and 3.2 respectively, we focus on the local region where both processes are taking place and compare the results before and after the events. In order to have a comprehensive picture, we also carry out full PRT calculations in Section 3.3, including effects such as absorption, emission, Faraday rotation and Faraday conversion.

3.1.1. *Enhanced RM magnitude Behind Shock Front*

We compare the RM values centered near the shock front at two different times: 1.6 Gyr, before any significant interaction occurs, and 2 Gyr, during the subcluster's passing. At 2 Gyr, we identify the tip of the shock front at approximately $[-1.1, -0.5, 0]$ Mpc where it appears as a bow-shaped, sharp discontinuity in the projected X-ray emissivity map along the z direction (see Figure 1, bottom right panel). This feature is observed in the energy band of 0.5–7 keV.

Figure 1 presents the RM maps before and after shock passing overlaid with projected X-ray contours in the right column, while the left displays the simulated projected X-ray emissivity along the z direction. We estimate general variation in RM magnitude in the post-shock region by evaluating the difference in | RM | before and after shock passage, averaging over space. The post-shock region is determined by the pixels enclosed by the X-ray contour marks at the level of 10^{-6}erg cm^{-2}s^{-1}. At 2 Gyr, the magnitude of RM behind the shock front has a local 7.8 rad m^{-2} increment on average over the chosen area, which is about a general 56.0% growth after the shock has passed through. This is also associated with larger fluctuations in RM, as its standard deviation increases from 18.0 to 30.3 rad m^{-2}. The increase in RM magnitude is expected, as both the jump in electron density and the compression of magnetic fields along the shock front enhance the local RM (M. Lyutikov 2006; R. J. van Weeren et al. 2010; L. Iapichino & M. Brüggen 2012; M. Brüggen et al. 2012).

3.1.2. *Enhanced Magnetic Field Strength Behind Shock Front*

Observations of the FD in the Fornax cluster reveal a depletion of polarized light sources between possible locations of the shock front and the contact discontinuity (C. S. Anderson et al. 2021). This depolarized region consists of two distinct parts along the wings of the swept-back patches, curving concavely upward from the center marked by the X-ray contours of the central

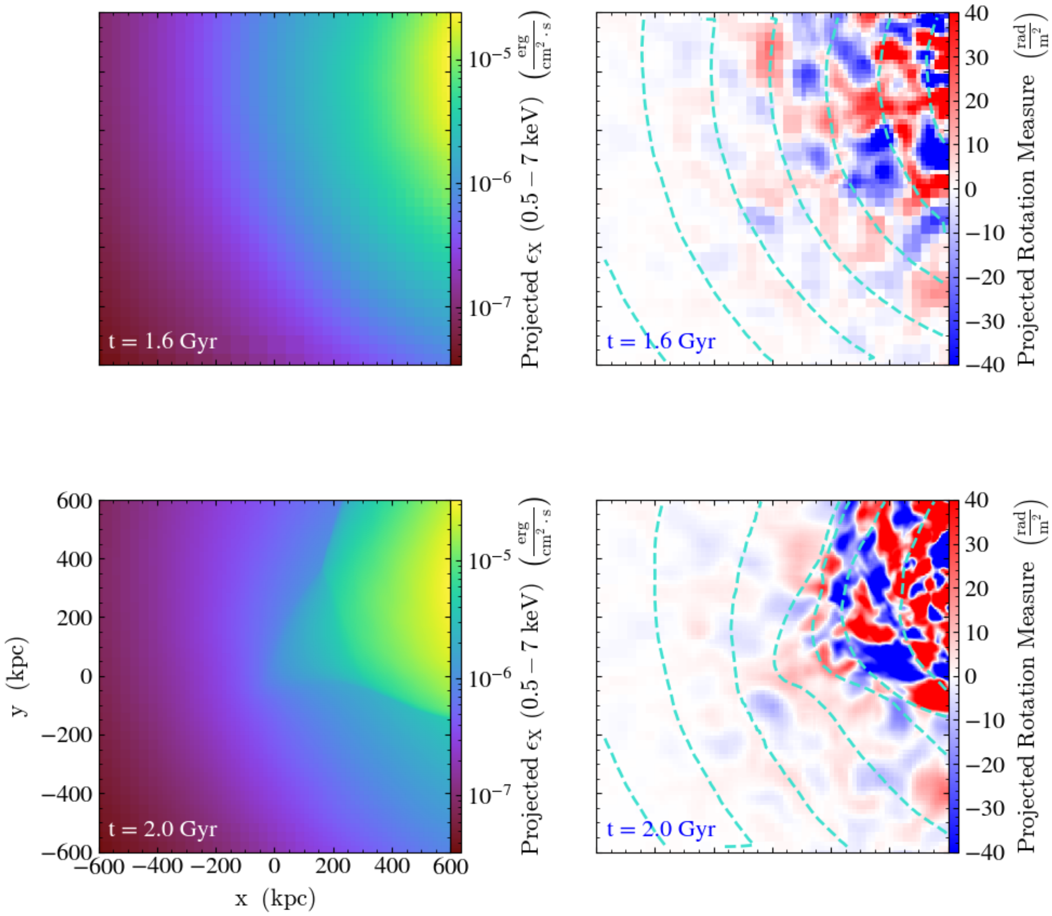

Figure 1. Projected X-ray emissivity in energy band 0.5 – 7 keV (left column) and RM (right column) zoomed-in towards the shock front at 1.6 Gyr (pre-shock; first row) and at 2 Gyr (post-shock; second row). Contours represent evenly-spaced X-ray surface brightness from -5 to -7.5, with a step size of $d = -0.5$ on a logarithmic scale. We find RM enhancement behind the shock front, while the depolarization effect is not apparent.

galaxy NGC 1399. This raises the question of whether the observed depletion results from depolarization, potentially caused by turbulence behind the shock front (B. J. Burn 1966; M. Murgia et al. 2004; A. Bonafede et al. 2010; J.-H. Ha et al. 2018; C. S. Anderson et al. 2021). In our simulation, the distinction between the shock front and the contact discontinuity is almost nonexistent. As shown in Figure 2, the subcluster that is identified as the point of lowest gravitational potential lies directly atop the shock front, and we observe no clear signs of depolarization.

In Figure 2, the magnetic field strength in the post-shock region is clearly enhanced, as indicated by the longer vectors compared to the ambient medium. While the field orientations appear somewhat disordered—a consequence of the initially tangled field structure and the relatively weak (low-Mach) shock—the overall enhancement is consistent with compression of the field component parallel to the shock front. Over time, this compressed field can evolve into turbulence as vorticity develops behind the shock. The realignment and amplification of the parallel field component are best visualized in three dimensions, and may not be readily apparent in a 2D slice plot.

3.1.3. *Polarization Fraction with Beam Smoothing*

We examine the effects of beam smoothing on the RM fluctuations across the sky plane before and after the passage of the shock. Before smoothing, we re-sample the AMR grid into a uniform grid with a pixel size of 31.25 kpc. This is because the shock front at 1.6 Gyr lies slightly off-center, and the resolution there is coarse before the shock passage. We therefore re-grid

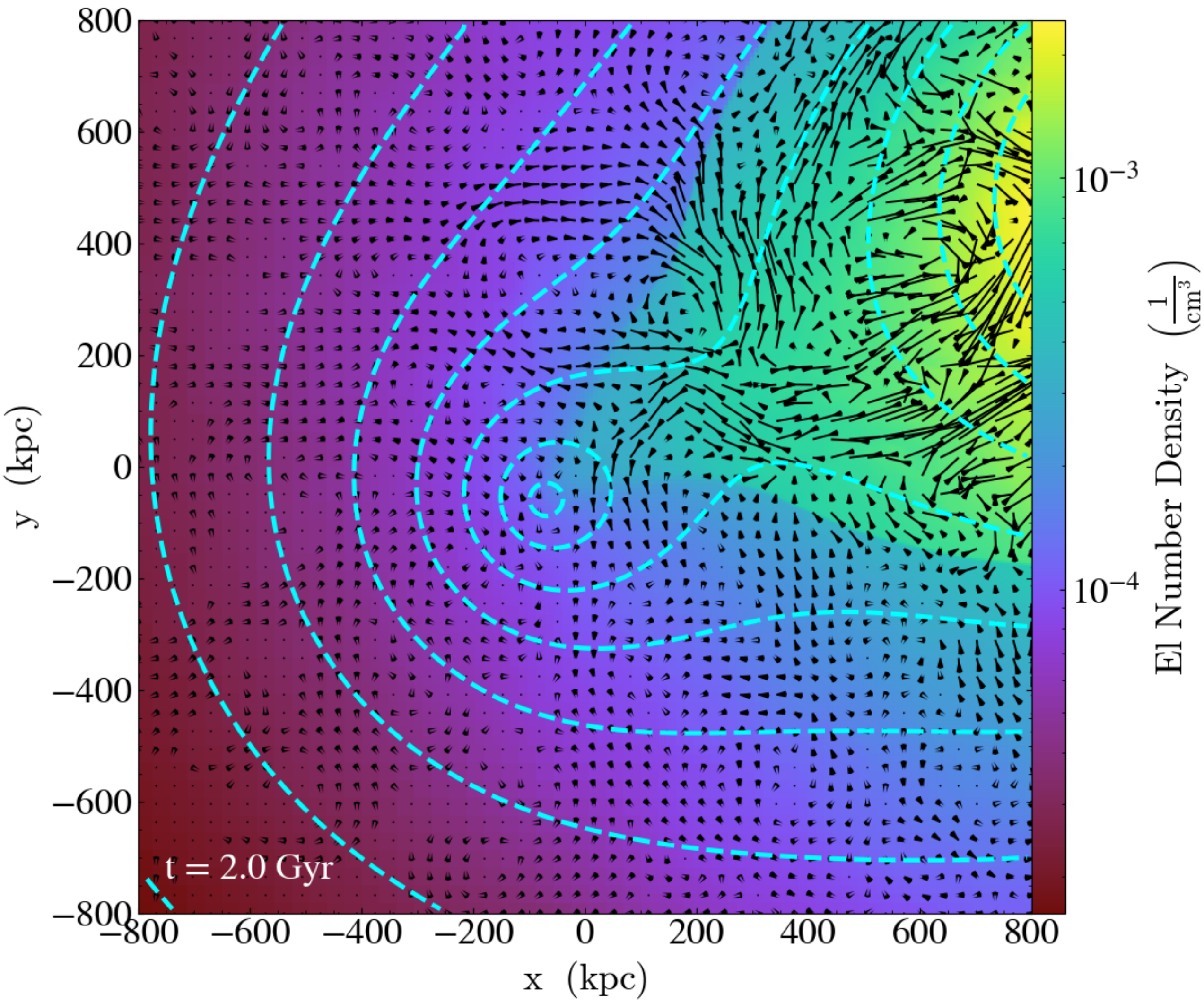

Figure 2. Slice plot of gas density across the shock front, with gravitational potential contours (cyan dashed lines) overlaid with magnetic field vectors (black arrows). The subcluster's central position (dip in the gravitational potential) coincides with the tip of the shock front, indicating the lack of separation between the shock front and the contact discontinuity in our merger simulation.

the region around the shock before and after the shock passage to enable a fair comparison. Gaussian smoothing is then applied using 2D kernels characterized by their standard deviation σ, which we evolve through $\sigma = 0, 0.5, 1$ pixel.

The resulting DOLP of the shock region subject to different beam smoothing sizes are shown in Figure 3. In the first row at $\sigma = 0$ at 1.6 Gyr and 2 Gyr, the smoothed DOLP of the ICM is the same as the initial totally polarized background. This is because, at $\sigma = 0$, there is no beam smoothing, and the DOLP of the ICM is dominated by the 100% linearly-polarized background. In the middle and bottom rows, corresponding to smoothing kernels of $\sigma = 0.5$ and 1, the DOLP centered on the shock front decreases from approximately 0.7 to 0.3. This suggests that, as beam resolution worsens, the ability to resolve small-scale structures diminishes. The depolarized region traces the shock front more clearly at 2 Gyr compared to 1.6 Gyr. Notably, both profiles with larger smoothing kernels ($\sigma = 0.5$, 1) exhibit signs of depolarization even prior to the shock's arrival. This early depolarization is likely caused by fluctuations within the initially tangled magnetic field.

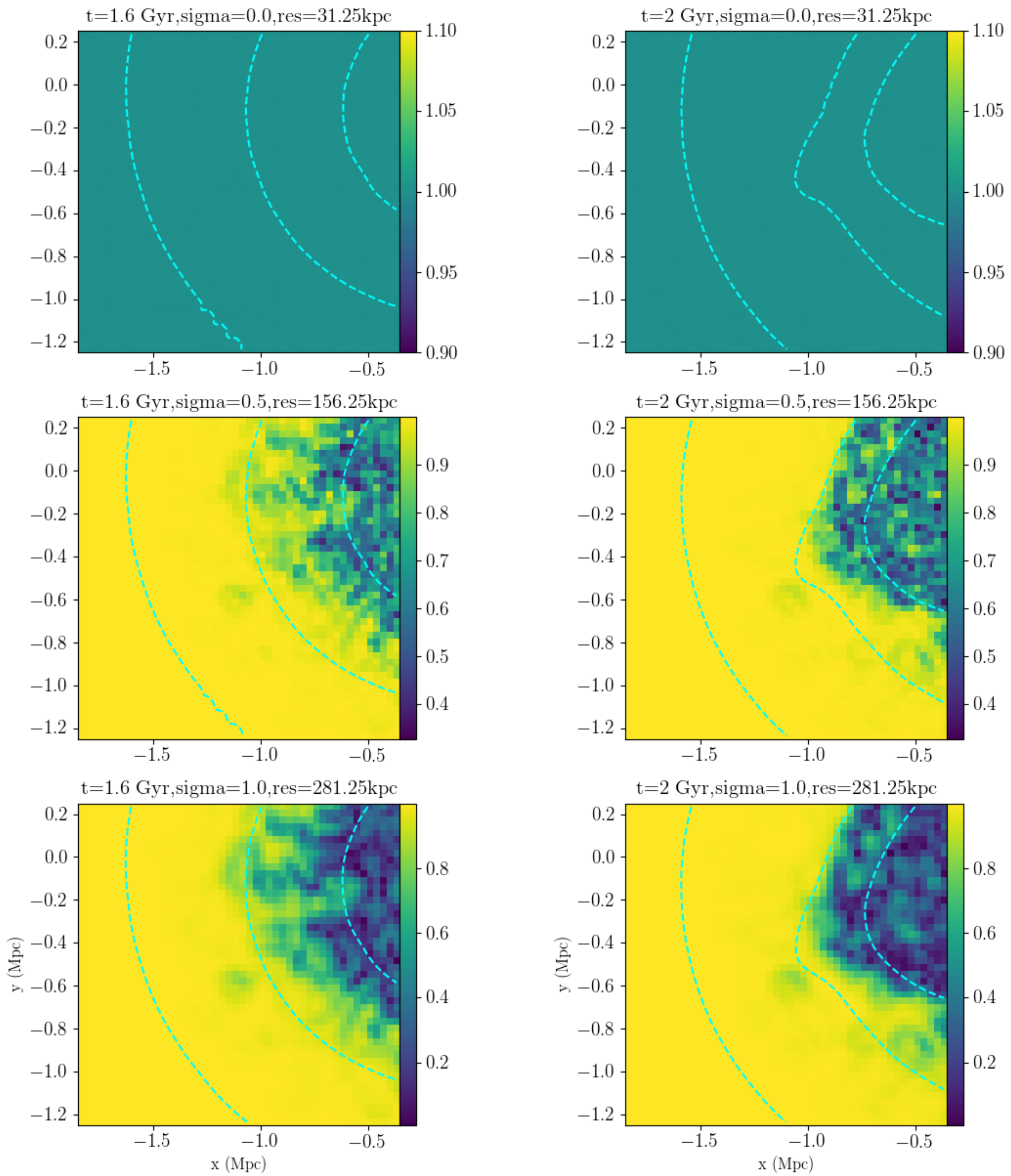

Figure 3. The left and right columns show DOLP maps at 1.6 Gyr (before shock passage) and 2 Gyr (after shock passage), respectively. The DOLP maps are smoothed by sigma (FWHM) of 0 (no smoothing; top row), 0.5×0.5 pixels (middle row) and 1×1 pixels (bottom row). The overlaid contours of X-ray surface brightness in cyan dashed lines represent evenly-spaced values from -5 to -7, with a step size of $d = -1$ on a logarithmic scale. Beam depolarization occurs behind the shock front due to an enhance in magnetic field fluctuations across the plane of the sky, with the effect becoming more pronounced as the beam size increases.

3.2. *Sloshing Scenario*

3.2.1. *Decreasing RM magnitude after Sloshing*

As gas sloshes around the cluster core, the sloshing motion may trigger turbulence near the center by Kelvin-Helmholtz instabilities at the interface of the cold front, or the mixing of layers of gas in the presence of a self-gravitational field by Rayleigh-Taylor instabilities. We examine the RM and projected X-ray emissivity maps near the cluster center at t = 1.2 Gyr at the onset of sloshing (Figure 4 top row); and at t = 2.7 Gyr during the sloshing motion (Figure 4 bottom row). According to G. B. Taylor et al. (2002) and C. L. Carilli & G. B. Taylor (2002), magnitudes of RM in cool-core clusters show an increasing trend with respect to their cooling rates. In our simulation, the highest RM magnitude goes up to more than 10^4 rad m^{-2}, corresponding to the cooling rate of more than a few hundred $M_{\odot} yr^{-1}$, which is consistent with the observations of cool-core clusters at about 100 $M_{\odot} yr^{-1}$ (A. C. Fabian 1994). In both X-ray maps at 1.2 Gyr and 2.7 Gyr, there is a swirling pattern at the center of the cold front, formed by a discontinuous jump in density. The sloshing region is highlighted by X-ray contours exceeding 10^{-3}erg $m^{-2}s^{-1}$, within which clumps of both positive and negative RM values at 2.7 Gyr appear to fragment into smaller structures. This fragmentation is accompanied by a drop in the average RM magnitude of -790.9 rad m^{-2}, representing a 23.3% decrease compared to the the average value at $t = 1.2$ Gyr.

3.2.2. *Magnetic Field Entanglement Near the Cluster Center*

The RM magnitude decreases near the cluster center during sloshing at 2.7 Gyr. Since the thermal electron number density increases radially towards the center (see Figure 4 left column), the large-scale RM decrement (see Figure 4 right column) must be attributed to the tangled nature of the cluster magnetic field. The average RM standard deviation dips near the center from 5122.5 to 3082.2 rad m^{-2}, implying that the cancellation of magnetic field z components lowers the fluctuation in RM along the Z direction. Turbulence and/or gas sloshing can stir the magnetic field, introducing tangled field lines and random field inversions. These effects lead to increased cancellation along the line of sight. Figure 5 shows the emergence of more fluctuations in magnetic field z components along the horizontal line cutting across the cluster center at ±200 kpc. The local decreases in RM magnitude likely arise from these small-scale magnetic field entanglement, which in turn may contribute to the depolarization of background light passing through the region.

3.2.3. *Lower Polarization Fraction in Cluster Core Revealed by Beam Smoothing*

In Figure 6, we examine the effects of beam depolarization on the polarization fraction across the sky plane before and after the onset of sloshing at 1.2 Gyr and 2.7 Gyr, respectively. The polarization fraction is calculated analytically using equation 9, where the AMR grid is re-sampled into a uniform grid with a pixel size of 7.81 kpc. We apply a Gaussian smoothing with standard deviation σ ranging from $0, 0.5$ to 1 pixel.

The smoothed polarization fraction maps zoomed-in at the cluster center before and after the onset of sloshing are shown in left and right columns of Figure 6, respectively. The first row corresponds to $\sigma = 0$ and shows totally polarized background light with no signals being smeared. The second and third rows correspond to $\sigma = 0.5$ and $\sigma = 1$, respectively. We notice that the beam-smoothed profile of the sloshing core shows a large, boxy depolarized region, which is likely an artifact of the lower effective resolution at that epoch and sparse sampling in the spherical grid. However, this does not significantly influence the key results described below. As the beam size increases, the level of polarization decreases, with the minimum value of DOLP dropping from 0.7 to about 0.3. The fourth row is also smoothed at $\sigma = 1$, similar to the third row, but observed at a higher frequency of 6 GHz. As expected, Faraday depolarization is less severe at a higher frequency (see e.g. D. D. Sokoloff et al. 1998; S. Sur et al. 2021), so the depolarization region extends over a smaller length scale at 6 GHz (fourth row) than at 1.4 GHz (third row). By reducing the beam depolarization effect at higher frequency, the depolarization shaped by the sloshing event brings forth a distinctive shape of a compressed cold front.

The lower polarization fraction at the cluster center before sloshing arises mainly from the initial fluctuations in the tangled magnetic fields (c.f. Figures 4 and 6). Figure 7 shows the polarization angles (PA) at 2.7 Gyr, which are calculated analytically using equations 4, 6 and 7. The angles flip randomly between positive and negative values, due to the steep RM gradients near the cluster center, where the RM magnitude can range from several hundred to several thousand rad m^{-2} across a few pixels. These gradients lead to significant variations in the FD along different lines of sight, which, in turn, results in a lower observed DOLP in Figure 6.

3.3. *Comparisons with a full polarized radiative transfer treatment*

In Sections 3.1 and 3.2, we calculated the RM and PA maps analytically, assuming that the cluster is optically thin and only undergoes Faraday rotation. These are reasonable assumptions in our case, as a back-of-envelope comparison of the normalized ht!

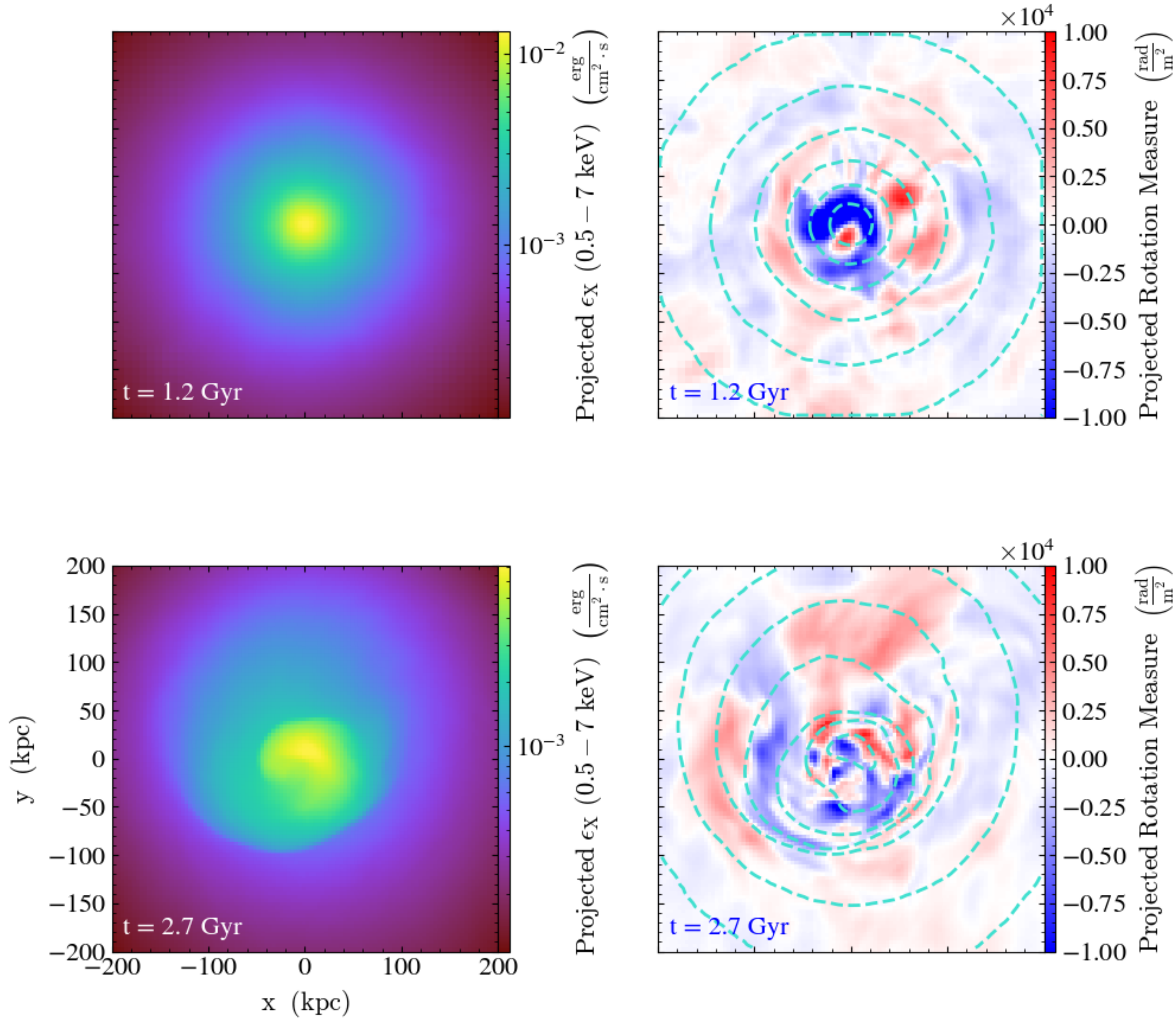

Figure 4. Projected X-ray emissivity in energy band 0.5 − 7 keV (left column) and RM (right column) zoomed-in towards the sloshing cold front at 1.2 Gyr (at the onset of sloshing; first row) and at 2.7 Gyr (after sloshing occurs; second row) Contours in the top and bottom panels represent evenly-spaced X-ray surface brightness from -2.1 to -3.6 and -2.5 to -3.75, with their respective step sizes being -0.3 and -0.25 on a logarithmic scale. The RM at cold front has in general decreased after sloshing occurs, as a result of strong magnetic field entanglement along the line of sight.

transfer coefficients near the cluster center gives $f' >> h' >> 1 >> \epsilon'_Q > q' >> \epsilon'_v > v'$ (see equation 2 in T. W. Jones & S. L. O'Dell 1977, for a summary). The Faraday rotation coefficient f' exceeds the convertibility coefficient h' by approximately an order of 10^7, and is about 10^{11} larger than the rest of the coefficients.

In reality, many merging clusters are complex systems, with a fraction of them hosting diffuse radio emission in the form of halos and/or relics. There can also be intervening synchrotron sources, such as radio galaxies embedded within the medium, which can absorb, emit and even Faraday convert the linearly-polarized light. In this section, we generalize our analyses to a broader range of conditions and carry out full PRT calculations of our merging cluster simulation, assuming a uniform background of radio point sources and compare the results to our analytical treatment.

ht!

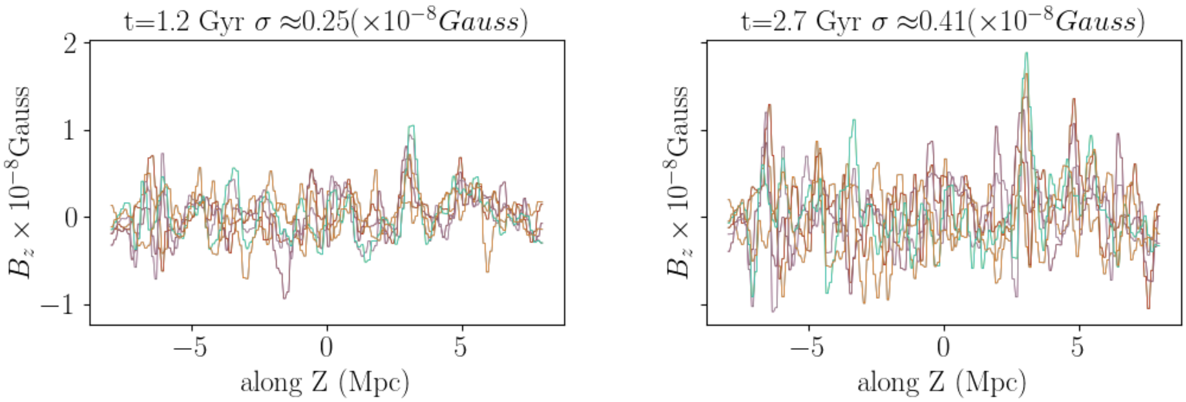

Figure 5. Spatial evolution of the magnetic field's Z component (B_z) along the Z axis, sampled across the X axis from $x = -200$ kpc to $x = 200$ kpc, with each color representing different line of sight. This region is experiencing sloshing motions. The left and right panels display B_z profiles at 1.2 Gyr and 2.7 Gyr, respectively. As sloshing progresses, the magnetic field becomes more tangled on smaller scales, as indicated by an increased standard deviation (σ) of B_z. This increased tangling leads to stronger cancellation effects in the RM.

run	background source				transfer coefficients					emission coefficients		
	I_0	Q_0	U_0	V_0	f	h	k	q	v	$\epsilon_{\rm I}$	$\epsilon_{\rm Q}$	$\epsilon_{\rm V}$
f1e0			0	0	on	off	off	off	off	off	off	off
f1e1	$10^{-(13-15)}$	$10^{-(13-15)}$	0	0	on	off	off	off	off	on	on	on
all1e1			0	0	on	on	on	on	on	on	on	on

Table 1. Set-up of the transfer and emission coefficients for thermal and non-thermal electrons, and the corresponding background source Stokes parameters used in the polarized radiative transfer (PRT) calculations. We vary the intensity I_0 from 10^{-13}, 10^{-14}, 10^{-15} erg s^{-1}cm^{-2}Hz^{-1}str^{-1} to simulate the different intensities in background light, while keeping them highly linearly polarized at 100% with $I_0 = Q_0$. For run f1e0, only the Faraday rotation coefficient is switched on, whereas all of the coefficients are turned on in run all1e1. In run f1e1, only Faraday rotation and emissivities $\epsilon_{\rm I,Q,V}$ are turned on.

3.3.1. *Consistent Synchrotron Emission and Polarization Angles with Analytical Treatment*

We manually implement the analytical form of synchrotron emissivity (Section 2.3). Figure 8 (left) shows the analytical 1.4 GHz total radio synchrotron sky map at 2.7 Gyr. By zooming in on the cluster center (right), we see spiral features from the sloshing motion, where the discontinuity at the underside of the spiral forms a cold front. For a comparison, we carried out a PRT calculation of the same system, without any background sources. Assuming that only emission and Faraday rotation are present, we calculated the total synchrotron intensity map (left) and polarization angle map (right) of the cluster at 2.7 Gyr in Figure 9. The analytical and PRT-computed synchrotron intensity maps (c.f. the left panels of Figures 8 and 9) and polarization angle maps (c.f. Figure 7 and the right panel of Figure 9) are consistent in terms of morphology and order of magnitude.

3.3.2. *Polarization Maps near the Sloshing Center with Varying Background Intensity or Varying Background DOLP*

We calculate 1.4 GHz mock radio observations of the merging cluster simulation at 2.7 Gyr towards a uniform distribution of background point sources. We vary the intensity of the background point sources I_0 from 10^{-13}, 10^{-14}, 10^{-15} erg s^{-1}cm^{-2}Hz^{-1}str^{-1}, which is about 100, 10 and 1 times the maximum synchrotron emission from the cluster itself. The background point sources are assumed to be totally linearly polarized at DOLP = 100%, with $I_0 = Q_0$. We set $U_0 = 0$, such that the initial polarization angle is fixed at $\varphi_0 = 0$ radian. The initial conditions of the uniform polarized background sources make it more transparent for us to keep track of any depolarization signatures due to the intervening ICM.

In Table 1, we consider three cases, where only Faraday rotation occurs (f1e0), both Faraday rotation and emission are present (f1e1), and all emission and transfer effects (including absorption and Faraday conversion) take place (all1e1). The DOLP maps are similar across cases f1e1 and all1e1, indicating that absorption and Faraday conversion are insignificant in our system. Figure 10 shows the DOLP maps for case all1e1, as the background intensity lowers from 10^{-13} (left), 10^{-14} (middle), to 10^{-15}

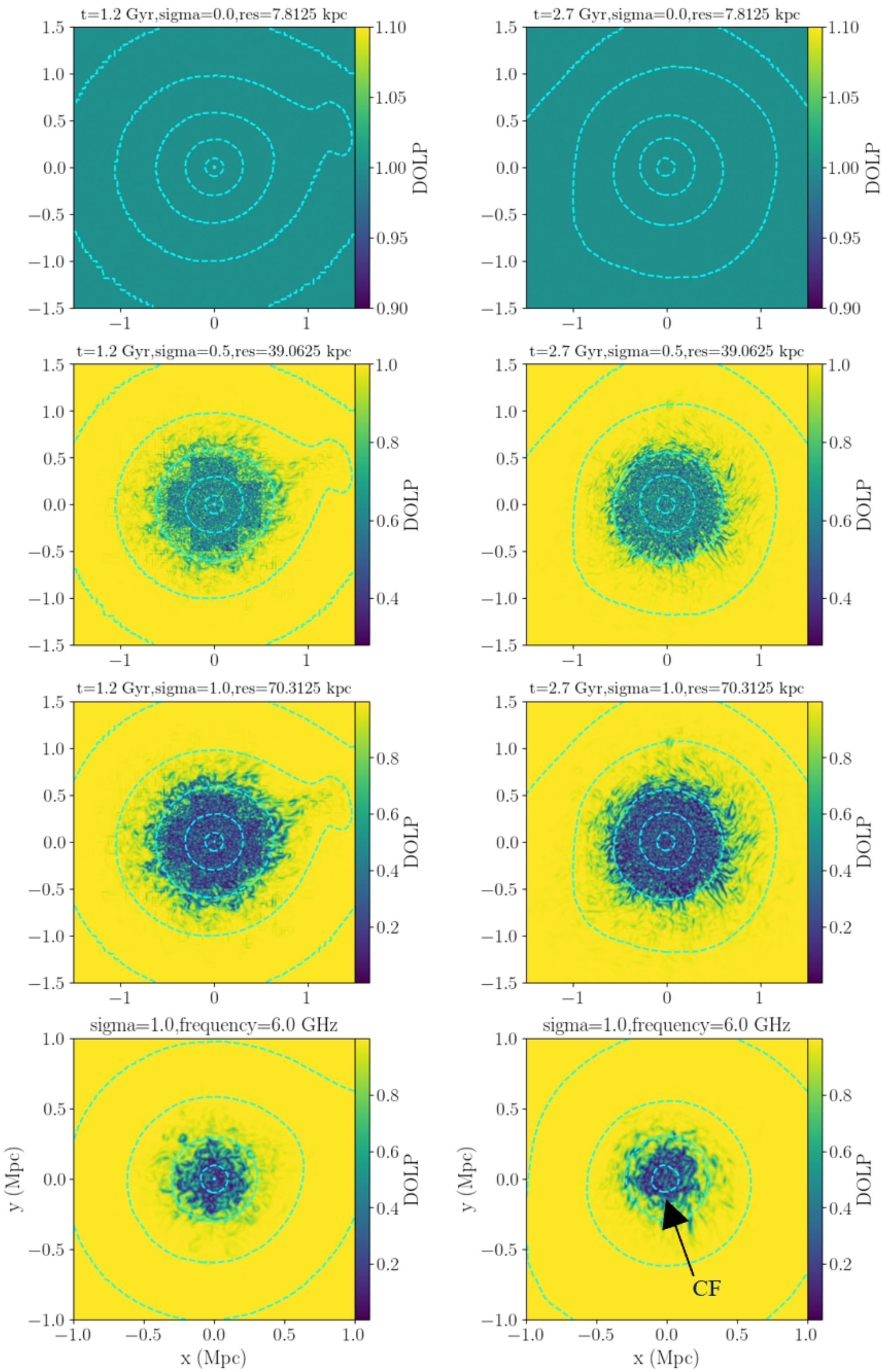

Figure 6. The first three rows show the DOLP maps smoothed by sigma (FWHM) values of 0 (no smoothing), 0.5×0.5, and 1×1 pixels, observed at 1.4 Gyr. The contours represent X-ray surface brightness starting at -3 at the center, decreasing by 1 with each step outwards on a logarithmic scale. The left and right columns show profiles at 1.2 Gyr (the onset of sloshing) and 2.7 Gyr (after sloshing occurs), respectively. The last row highlights depolarized regions at 6 GHz, smoothed with 1×1 pixels and zoomed in on the 500 kpc central region. Beam depolarization occurs at the sloshing center due to enhanced magnetic field fluctuations, becoming more pronounced as beam size increases from rows 1 to 3. The depolarization area is similar between 1.2 Gyr and 2.7 Gyr, due to the initially tangled magnetic field. Comparing between rows 3 and 4, the central region is more depolarized at 1.4 GHz than at 6 GHz, due to Faraday depolarization being more severe at lower frequencies. The compressed cold front (CF) is visible after sloshing at 6 GHz.

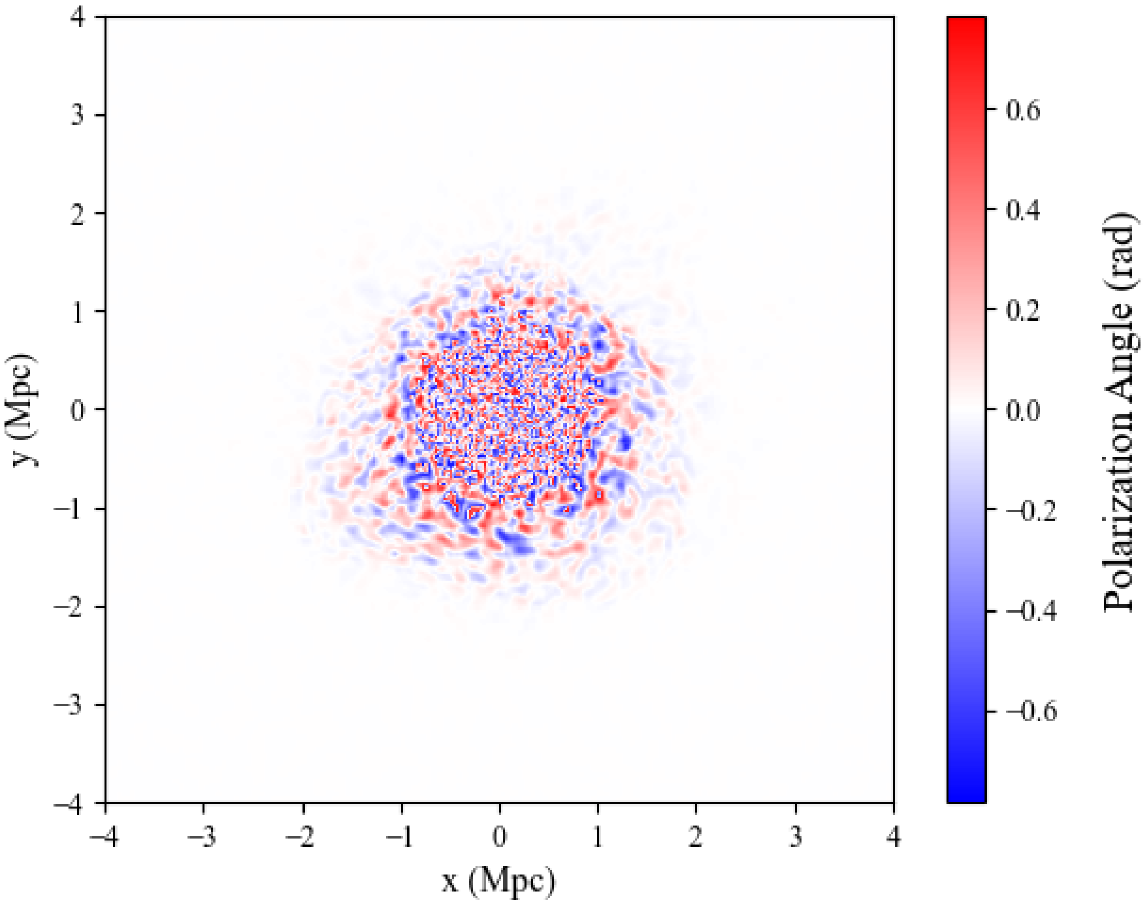

Figure 7. Semi-analytical map of the polarization angles encompassing the whole cluster at 2.7 Gyr. The center exhibits a criss-cross pattern of angles flipping between positive and negative values, resulting from the high RM in that region.

$\mathrm{erg\,s^{-1}cm^{-2}Hz^{-1}str^{-1}}$ (right). The depolarization effect becomes more pronounced as the background intensity decreases to a similar level as the cluster emission. This is consistent with the depolarization conditions identified in A. Y. L. On et al. (2025), where the dim sources are depolarized by different amounts, depending on the location of the sources and the magneto-ionic properties of the cluster.

To quantify how the observed polarization fraction changes with initial source DOLP, we set a uniform background total intensity of $I_0 = 10^{-15}\mathrm{erg\,s^{-1}Hz^{-1}cm^{-2}str^{-1}}$, while varying the initial DOLP from 5%, 20% to 100%. Figure 11 shows the resulting polarization maps zoomed in on the cluster center. As the DOLP of the background sources increases (from left to right), most cluster sources exhibit a corresponding rise in polarization fraction. A notable depolarization, emerges near a radius of approximately 500 kpc. In the left and middle panels, however, several pixels stand out with noticeably higher polarization values compared to their local surroundings. These pixels do not undergo depolarization; instead, their observed DOLP is larger than their initial DOLP. This enhancement is physical, and it occurs when the polarization fraction of the ICM exceeds that of the background light, mainly due to larger electron number densities and stronger, more aligned magnetic fields near the cluster center (see also A. Y. L. On et al. 2025, for polarization enhancement conditions). In general, the number of enhanced pixels decreases as the background DOLP increases.

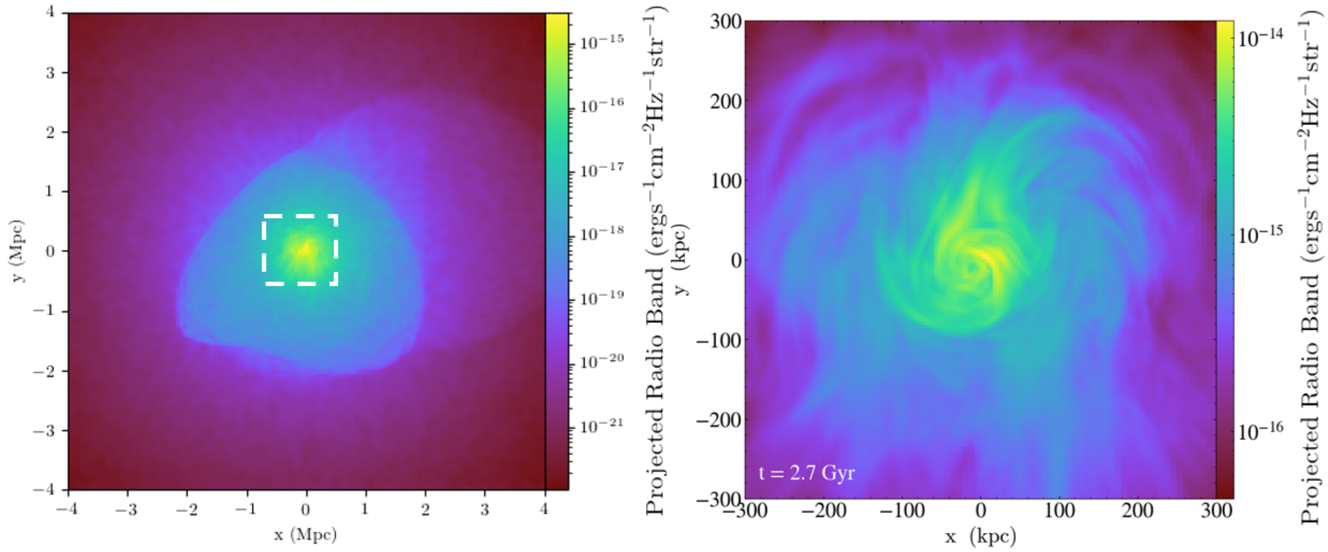

Figure 8. The left panel shows the analytical 1.4 GHz radio synchrotron sky map at 2.7 Gyr. The right panel shows the synchrotron emission zoomed in on the cluster center (white dashed box), showing the sloshing pattern which traces the structures of the transverse component of the magnetic field.

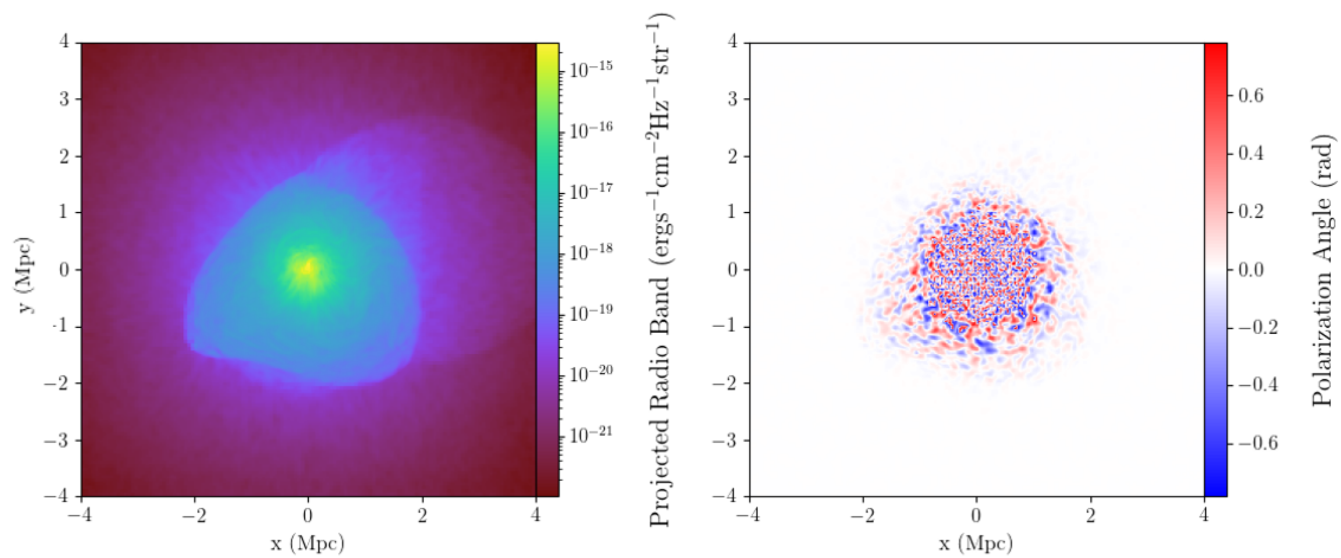

Figure 9. The total synchrotron intensity map (left panel) and polarization angle map (right) of the cluster at 2.7 Gyr generated using PRT calculations, assuming that only emission coefficient ϵ_I and the Faraday rotation coefficient f are turned on. The analytically-implemented and PRT-computed synchrotron and polarization angle signatures (c.f. Figure 7) are consistent.

4. DISCUSSION

4.1. *Comparison between the shock and sloshing features in our simulations*

Both shock and sloshing are able to cause fluctuations in the magnetic field lines. From the beam smoothed DOLP maps in Figure 3 and Figure 6, both occurrences lead to beam depolarization behind the shock/cold front, respectively. The overall DOLP follows a general trend as it decreases from roughly 0.7 to 0.3 with a larger beam size. The extra frequency observed at 6 GHz reveals a more distinct shape of the sloshing cold front because the fluctuations in FD diminish with higher frequency (shorter wavelength).

The morphologies and the change in the RM magnitude due to shock and sloshing are quite different, however. There is an asymmetric, bow-shaped enhancement of approximately 56.0% in the selected region for the RM behind the shock front in our

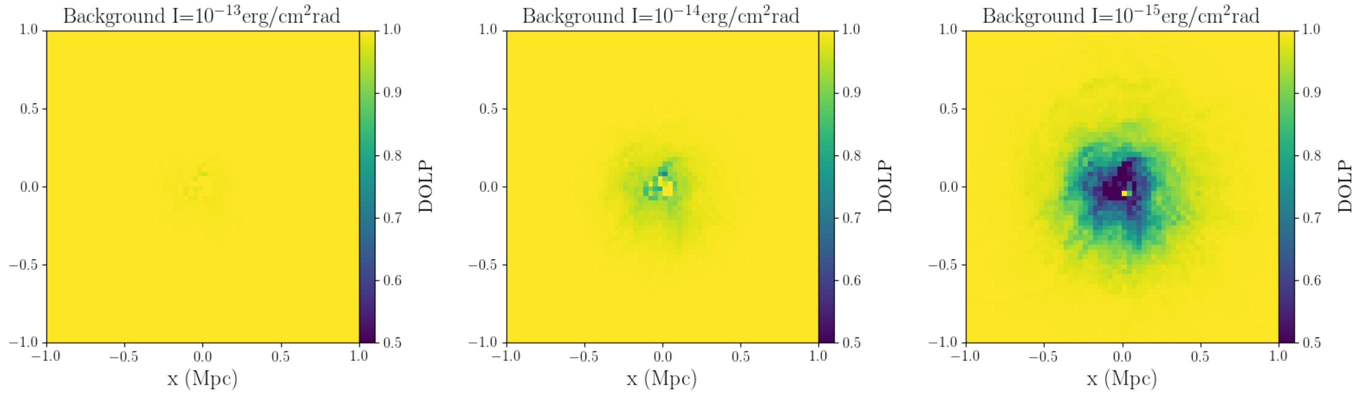

Figure 10. DOLP maps solved by the PRT code with all coefficients turned on, focusing on the sloshing center. From left to right, the initial background intensity I is uniform at 10^{-13}, 10^{-14}, and 10^{-15} erg s^{-1}Hz^{-1} cm^{-2} str^{-1}, respectively. We find that uniform background light is more depolarized near the cluster center, with this effect becoming more pronounced as background intensity decreases. There are a few pixels near the center where their values are unusually high (the yellow pixel located slightly offset in a sea of green pixels), which could be due to numerical errors.

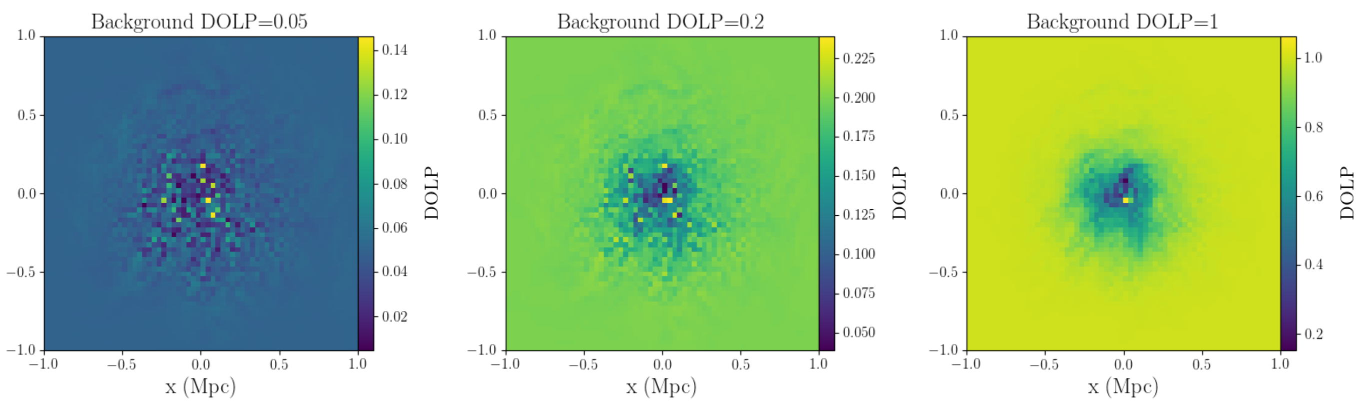

Figure 11. DOLP maps solved by the PRT code with all coefficients turned on, focusing on the sloshing center. The initial background intensity is set to 10^{-15}erg s^{-1}Hz^{-1}cm^{-2}str^{-1}, while the DOLP varies from 5%, 20% to 100% from left to right. We find that uniform background light is sometimes enhanced near the cluster center, with this effect becoming more pronounced as background DOLP decreases.

simulation, due to the compression in gas and magnetic field lines after shock passing (Figure 1). On the other hand, the sloshing motions generate a spiral pattern in the RM around the cluster center, and have generally lower magnitude of RM within the inner radius of 100 kpc . There is a 23.3% decrease with respect to the initial RM magnitude (Figure 4).

4.2. *Comparison between our simulation results and observations*

The morphologies in the X-ray and RM maps near the shock front in our simulation (Figure 1) closely resemble some of the features seen in observations (C. S. Anderson et al. 2021). The X-ray morphology is disturbed in Figure 1 (left column), clearly tracing the merger axis in the NE - SW direction as the subcluster falls into the main cluster, with X-ray emission brightening behind the wake. The projected RMs in our simulation are also visibly higher in the post-shock region and extend over Mpc scales, which are similar to the Fornax observations. On the other hand, the RM maps in Figure 4 (right column) show that sloshing motions can randomize magnetic field lines, causing the RM to change signs on small scales. It is therefore possible for turbulence to result in the isotropic distribution of RMs seen behind the wake in the Fornax cluster.

There are a few differences between our simulations and observations. In our simulation, there is no distinct separation between the contact discontinuity (the edge of the subcluster) and the shock front (see Figure 2). This means that we cannot assess whether there is depolarization or a lack of polarized sources between the area enclosed by the contact discontinuity and the bow shock, as proposed in C. S. Anderson et al. (2021). In addition, our shock has a smaller opening angle at $\sim 30°$ with a larger Mach number at $M_s \approx 2$ than in the Fornax observation. Having a stronger shock in our simulation may lead to a larger RM enhancement in the post-shock region.

Our simulation does not include viscosity, and it is therefore more susceptible to hydrodynamic instabilities. If viscosity is taken into account, it would suppress turbulence in the ICM, leading to less fluctuations in the RMs. Moreover, viscosity is also an important factor to stabilize cold fronts. As such, it is possible to delay the onset of turbulence near the sloshing center, affecting the level at which the RM magnitude changes in our simulation.

5. CONCLUSIONS

We carried out analytical and full PRT calculations of radio point sources behind a merging galaxy cluster from the FLASH simulations to investigate the reasons behind depolarization seen in the recent Fornax cluster observations. Our main results are summarized below.

1. The projected RMs in our post-shock region have a similar morphology to the Fornax observations. The RMs are visibly higher. There is an $\approx 56\%$ increase in RM magnitude in the region behind the shock front, which extends over Mpc scales. The enhancement along the shock front likely arises from the compression of hot gas and magnetic field lines in our simulation. The X-ray contours in our simulation follow a swept-back morphology along the cluster merger axis, which is comparable to the X-ray observations of the Fornax cluster.

2. The sloshing core within a radius of a few hundred kpc shows a decrease in RM magnitude by $\approx 23.3\%$ in the affected region, due to the tangled magnetic field induced by sloshing-driven turbulence.

3. The smoothed DOLP of shock front and sloshing center reveal small-scale, unresolved structures depolarizing the background sources. The beam depolarization region extends around the shock front and the cold front.

4. By incorporating all relevant radiative transfer coefficients into the PRT calculations, we find that the DOLP of the ICM exhibits more pronounced depolarization features near the cluster center as the background source intensity decreases. For a constant background intensity, the number of pixels with enhanced polarization increases with diminishing initial background DOLP. These findings underscore how synchrotron emission and Faraday rotation within the intervening ICM significantly modulate the observed polarization of background radio sources.

While there is no clear indication from our simulations as to why there is a lack of polarized radio sources in the Fornax cluster field, our work demonstrates that deep, wide-field RM and polarization grids are valuable means to better understand the magneto-ionic properties of the ICM.

ACKNOWLEDGEMENTS

JRL and HYKY acknowledge support from National Science and Technology Council (NSTC) of Taiwan (NSTC 112-2628-M-007-003- MY3; NSTC 114-2112-M-007-032-MY3). HYKY acknowledges support from Yushan Scholar Program of the Ministry of Education (MoE) of Taiwan (MOE-108- YSFMS-0002-003-P1). AYLO is supported by the NSTC of Taiwan through the grants 111-2124-M-002-013-, 112-2124-M-002-003- and 113-2124-M-002-003-, the MoE (Higher Education Sprout Project NTU-113L104022-1) and the National Center for Theoretical Sciences of Taiwan. This work used high-performance computing facilities operated by Center for Informatics and Computation in Astronomy (CICA) at National Tsing Hua University (NTHU). This equipment was funded by the MoE of Taiwan, the NSTC of Taiwan, and NTHU. FLASH was developed in part by the DOE NASA- and DOE Office of Science-supported Flash Center for Computational Science at the University of Chicago and the University of Rochester. The PRT code was developed in-house at the Mullard Space Science Laboratory in University College London (see A. Y. L. On et al. 2019; J. Y. H. Chan et al. 2019). Data analysis presented in this paper was conducted with the publicly available yt visualization software (M. J. Turk et al. 2011), astropy (Astropy Collaboration et al. 2022) and Google Colab. We are grateful to the yt development team and community for their support. Support for JAZ was provided by the *Chandra* X-ray Observatory Center, which is operated by the Smithsonian Astrophysical Observatory for and on behalf of NASA under contract NAS8-03060. AYLO thanks Dr. Jennifer Y. H. Chan (Dunlap/CITA), Paul C. W. Lai (MSSL/UCL), Prof. Kinwah Wu (MSSL/UCL), Dr. Ziri Younsi (MSSL/UCL), Kaye Li (MSSL/UCL) and Prof. Hung-Yi Pu (NTNU) for technical discussions on the PRT code during various stages of this work. AYLO also acknowledges the international conferences on Cosmic Magnetism in the Pre-SKA Era 2024 in Kagoshima and the Cosmic Magnetism with Radio Astronomy 2024 in Pisa for discussions on depolarization in galaxy clusters, in particular with Dr. Erik Osinga (Dunlap), Dr. Craig Anderson (ANU), Dr. Francesca Loi (INAF-OAC), Dr. Yik Ki Jackie Ma (MPIfR), Dr. Aritra Basu (TLS) and Dr. Juan D. Soler (IAPS-INAF). This research has made use of NASA's Astrophysics Data Systems.

DATA AVAILABILITY

The data underlying this article will be shared on reasonable request to the corresponding authors.

Facilities: HST(STIS), Swift(XRT and UVOT), AAVSO, CTIO:1.3m, CTIO:1.5m, CXO

REFERENCES

Anderson, C. S., Heald, G. H., Eilek, J. A., et al. 2021, PASA, 38, e020, doi: 10.1017/pasa.2021.4

Barnes, D. J., On, A. Y. L., Wu, K., & Kawata, D. 2018, MNRAS, 476, 2890, doi: 10.1093/mnras/sty400

Bîrzan, L., Rafferty, D. A., Nulsen, P. E. J., et al. 2012, MNRAS, 427, 3468, doi: 10.1111/j.1365-2966.2012.22083.x

Bonafede, A., Feretti, L., Murgia, M., et al. 2010, A&A, 513, A30, doi: 10.1051/0004-6361/200913696

Brüggen, M., Bykov, A., Ryu, D., & Röttgering, H. 2012, SSRv, 166, 187, doi: 10.1007/s11214-011-9785-9

Burn, B. J. 1966, MNRAS, 133, 67, doi: 10.1093/mnras/133.1.67

Carilli, C. L., & Taylor, G. B. 2002, ARA&A, 40, 319, doi: 10.1146/annurev.astro.40.060401.093852

Chan, J. Y. H., Wu, K., On, A. Y. L., et al. 2019, MNRAS, 484, 1427, doi: 10.1093/mnras/sty3498

Clarke, T. E., Kronberg, P. P., & Böhringer, H. 2001, ApJL, 547, L111, doi: 10.1086/318896

Davies, J. I., Bianchi, S., Baes, M., et al. 2013, MNRAS, 428, 834, doi: 10.1093/mnras/sts082

Dreher, J. W., Carilli, C. L., & Perley, R. A. 1987, ApJ, 316, 611, doi: 10.1086/165229

Drinkwater, M. J., Gregg, M. D., & Colless, M. 2001, ApJL, 548, L139, doi: 10.1086/319113

Dubey, A., Reid, L. B., Weide, K., et al. 2009, arXiv e-prints, arXiv:0903.4875, doi: 10.48550/arXiv.0903.4875

Eddington, A. S. 1916, MNRAS, 76, 572, doi: 10.1093/mnras/76.7.572

Fabian, A. C. 1994, ARA&A, 32, 277, doi: 10.1146/annurev.aa.32.090194.001425

Ferland, G. J., Porter, R. L., van Hoof, P. A. M., et al. 2013, RMxAA, 49, 137, doi: 10.48550/arXiv.1302.4485

Ferrari, C., Govoni, F., Schindler, S., Bykov, A. M., & Rephaeli, Y. 2008, SSRv, 134, 93, doi: 10.1007/s11214-008-9311-x

Fryxell, B., Olson, K., Ricker, P., et al. 2000, ApJS, 131, 273, doi: 10.1086/317361

Govoni, F., Dolag, K., Murgia, M., et al. 2010, A&A, 522, A105, doi: 10.1051/0004-6361/200913665

Ha, J.-H., Ryu, D., & Kang, H. 2018, ApJ, 857, 26, doi: 10.3847/1538-4357/aab4a2

Heald, G. 2009, in IAU Symposium, Vol. 259, Cosmic Magnetic Fields: From Planets, to Stars and Galaxies, ed. K. G. Strassmeier, A. G. Kosovichev, & J. E. Beckman, 591–602, doi: 10.1017/S1743921309031421

Hutschenreuter, S., Anderson, C. S., Betti, S., et al. 2022, A&A, 657, A43, doi: 10.1051/0004-6361/202140486

Iapichino, L., & Brüggen, M. 2012, MNRAS, 423, 2781, doi: 10.1111/j.1365-2966.2012.21084.x

Jones, C., Stern, C., Forman, W., et al. 1997, ApJ, 482, 143, doi: 10.1086/304104

Jones, T. W., & O'Dell, S. L. 1977, ApJ, 214, 522, doi: 10.1086/155278

Keshet, U., Markevitch, M., Birnboim, Y., & Loeb, A. 2010, ApJL, 719, L74, doi: 10.1088/2041-8205/719/1/L74

Kotarba, H., Lesch, H., Dolag, K., et al. 2011, MNRAS, 415, 3189, doi: 10.1111/j.1365-2966.2011.18932.x

Loi, F., Serra, P., Murgia, M., et al. 2025, A&A, 694, A125, doi: 10.1051/0004-6361/202451711

Lyutikov, M. 2006, MNRAS, 373, 73, doi: 10.1111/j.1365-2966.2006.10835.x

Machacek, M., Dosaj, A., Forman, W., et al. 2005, ApJ, 621, 663, doi: 10.1086/427548

Machacek, M. E., Nulsen, P., Stirbat, L., Jones, C., & Forman, W. R. 2005, ApJ, 630, 280, doi: 10.1086/431944

Mitton, S. 1971, MNRAS, 153, 133, doi: 10.1093/mnras/153.2.133

Murgia, M., Govoni, F., Feretti, L., et al. 2004, A&A, 424, 429, doi: 10.1051/0004-6361:20040191

Navarro, J. F., Frenk, C. S., & White, S. D. M. 1997, ApJ, 490, 493, doi: 10.1086/304888

On, A. Y. L., Chan, J. Y. H., Lai, P. C. W., & Wu, K. 2025, PASA, under review

On, A. Y. L., Chan, J. Y. H., Wu, K., Saxton, C. J., & van Driel-Gesztelyi, L. 2019, MNRAS, 490, 1697, doi: 10.1093/mnras/stz2683

Pacholczyk, A. G. 1970, Radio astrophysics: Nonthermal processes in galactic and extragalactic sources, Series of Books in Astronomy and Astrophysics (W. H. Freeman and Company, San Francisco), 77–111

Pacholczyk, A. G. 1977, Int. Series in Natural Philosophy, Vol. 89, Radio galaxies: Radiation transfer, dynamics, stability and evolution of a synchrotron plasmon (Pergamon Press, Oxford, New York, Toronto, Sydney, Paris, Frankfurt), 83–123

Roediger, E., & Zuhone, J. A. 2012, MNRAS, 419, 1338, doi: 10.1111/j.1365-2966.2011.19794.x

Ryu, D., Kang, H., Hallman, E., & Jones, T. W. 2003, ApJ, 593, 599, doi: 10.1086/376723

Scharf, C. A., Zurek, D. R., & Bureau, M. 2005, ApJ, 633, 154, doi: 10.1086/444531

Schuecker, P., Finoguenov, A., Miniati, F., Böhringer, H., & Briel, U. G. 2004, A&A, 426, 387, doi: 10.1051/0004-6361:20041039

Sheardown, A., Roediger, E., Su, Y., et al. 2018, ApJ, 865, 118, doi: 10.3847/1538-4357/aadc0f

Shurkin, K., Dunn, R. J. H., Gentile, G., Taylor, G. B., & Allen, S. W. 2008, MNRAS, 383, 923, doi: 10.1111/j.1365-2966.2007.12651.x

Simard-Normandin, M., & Kronberg, P. P. 1980, ApJ, 242, 74, doi: 10.1086/158445

Sokoloff, D. D., Bykov, A. A., Shukurov, A., et al. 1998, MNRAS, 299, 189, doi: 10.1046/j.1365-8711.1998.01782.x

Su, Y., Nulsen, P. E. J., Kraft, R. P., et al. 2017a, ApJ, 847, 94, doi: 10.3847/1538-4357/aa8954

Su, Y., Kraft, R. P., Roediger, E., et al. 2017b, ApJ, 834, 74, doi: 10.3847/1538-4357/834/1/74

Su, Y., Nulsen, P. E. J., Kraft, R. P., et al. 2017, The Astrophysical Journal, 851, 69, doi: 10.3847/1538-4357/aa989e

Sur, S., Basu, A., & Subramanian, K. 2021, MNRAS, 501, 3332, doi: 10.1093/mnras/staa3767

Taylor, G. B., Fabian, A. C., & Allen, S. W. 2002, MNRAS, 334, 769, doi: 10.1046/j.1365-8711.2002.05555.x

Turk, M. J., Smith, B. D., Oishi, J. S., et al. 2011, ApJS, 192, 9, doi: 10.1088/0067-0049/192/1/9

van Weeren, R. J., Röttgering, H. J. A., Brüggen, M., & Hoeft, M. 2010, Science, 330, 347, doi: 10.1126/science.1194293

Widrow, L. M. 2002, Reviews of Modern Physics, 74, 775, doi: 10.1103/RevModPhys.74.775

ZuHone, J. A., Markevitch, M., & Lee, D. 2011, ApJ, 743, 16, doi: 10.1088/0004-637X/743/1/16

ZuHone, J. A., Markevitch, M., Ruszkowski, M., & Lee, D. 2013, ApJ, 762, 69, doi: 10.1088/0004-637X/762/2/69